

Precision-Engineered Plasmonic Nanostar Arrays for High-Performance SERS Sensing

Alexandre Chícharo,* Alexandra Teixeira, Diogo Moreira, Maria S. Relvas, Marta Aranda, Temple Douglas, Jerôme Borme, Jana B. Nieder, Lorena Diéguez, and Sara Abalde-Cela*

Surface-enhanced Raman scattering (SERS) spectroscopy has emerged as a powerful tool for ultrasensitive and rapid analysis, with applications across several fields. The core mechanism of SERS is the interaction between molecules and plasmonic nanostructures, where localized surface plasmon resonances induce strong electromagnetic fields resulting in remarkable enhancements of Raman signals. The effectiveness of SERS substrates depends on their ability to generate strong electromagnetic fields at nanoscale hot spots, but achieving both reliable enhancement and reproducibility remains a challenge. This work presents a novel SERS substrate that combines a top-down fabrication approach with bottom-up wet chemistry to obtain an array of nanostars. Using electron beam lithography (EBL), uniform nanodisk arrays are first created, providing a controlled template. A subsequent chemical transformation reshapes these structures into nanostars, introducing sharp protrusions that significantly intensify localized electromagnetic fields. Finite-difference time-domain (FDTD) shows that nanodisks produce weak, symmetric field enhancements, while nanostars generate intense, highly localized electric fields at their spikes. Experimental SERS measurements using 1-naphthalenethiol (1-NAT), and tryptophan validate this transformation, demonstrating notable signal amplification with nanostar substrates. This work introduces a scalable and reproducible fabrication method for high-performance plasmonic SERS substrates, paving the way for a wide range of applications in distinct fields.

A. Chícharo, A. Teixeira, D. Moreira, M. S. Relvas, M. Aranda, T. Douglas, J. Borme, J. B. Nieder, L. Diéguez, S. Abalde-Cela International Iberian Nanotechnology Laboratory (INL) Avda. Mestre José Veiga, Braga 4715-310, Portugal E-mail: alexandre.chicharo@inl.int; sara.abalde@inl.int

A. Chícharo
Department of Chemistry
Humboldt-Universität zu Berlin
Newtonstr. 15, 12489 Berlin, Germany

The ORCID identification number(s) for the author(s) of this article can be found under https://doi.org/10.1002/adom.202501275

© 2025 The Author(s). Advanced Optical Materials published by Wiley-VCH GmbH. This is an open access article under the terms of the Creative Commons Attribution License, which permits use, distribution and reproduction in any medium, provided the original work is properly cited.

DOI: 10.1002/adom.202501275

1. Introduction

Surface-enhanced Raman scattering (SERS) spectroscopy is a powerful analytical technique that offers enhanced Raman signal intensity when compared to traditional Raman scattering due to the presence of localized surface plasmon resonances (LSPRs) in metallic nanostructures. This technique offers signal enhancements that often exceed conventional Raman scattering by several orders of magnitude, enabling applications ranging from singlemolecule detection to the investigation of intricate chemical processes at the nanoscale.[1,2] Seminal works by Kneipp et al. $(1997)^{[2]}$ and Moskovits $(1985)^{[3]}$ aid the foundation for single-molecule detection, broadening the applicability of SERS. SERS is considered a powerful tool with potential in diverse areas like medical diagnostics, biomedical diagnostics, environmental monitoring, and material characterization.[1,4,5] However, the ability to engineer and optimize SERS-active plasmonic substrates is essential for improving detection limits, enhancing reproducibility, and expanding the practical applications of the technique.[1,6]

Plasmonic nanostructures, including colloidal nanoparticles, engineered nanogaps, and periodic metallic arrays,

have been extensively studied to optimize SERS performance.^[7] Among these, periodic (plasmonic) arrays are known to sustain collective plasmon resonances,[8] leading to tunable optical properties beneficial for sensing applications. [9] These structures can exhibit collective plasmonic modes with long-range plasmonic coupling, resulting in narrow spectral features that are advantageous for specific detection applications. [8] Compared to nanodisks, nanostars, due to their multiple sharp tips and branched morphology, exhibit a higher density of electromagnetic hot spots, leading to improved SERS performance and sensitivity,[9-11] even when integrated into periodic arrays.[9] Despite recent advances in SERS substrates engineering, reproducibility and scalability remain significant challenges, blocking practical application of SERS technologies. [12] Many conventional SERS substrates, including self-assembled nanoparticle and chemically synthesized nanostars, exhibit structural variations



www.advopticalmat.de

that limit their uniformity and large-scale applicability.^[12] To overcome these challenges, alternative top-down approaches such as electron beam lithography (EBL) have gained interest, leveraging nanofabrication techniques to craft solid substrates with a high degree of control over nanoparticle geometry, arrangement, and size distribution, allowing the production of highly reproducible plasmonic nanostructures.^[7] Solid substrates have gained attention not only for their precision but also for their potential to revolutionize the field of SERS.^[7,13] They offer particle stability, a higher reproducibility from batch-to-batch as well as the possibility of washing steps while doing biochemical or complex matrixes analyses.

This study employs a top-down approach to first fabricate periodic gold nanodisks followed by their epitaxial growth into anchored nanostars using wet chemistry. This strategy combines the advantages of well-defined periodicity with the enhanced field confinement observed in star-shaped structures. It also addresses a critical challenge commonly found in solid substrate fabrication with techniques like EBL, namely the high cost and time-consuming nature of techniques like EBL, by implementing a more cost-efficient patterning approach, the dots-on-the-fly (DOTF) method, that maintains precision while significantly reducing processing time and overall expense.

Thus, the goal is to enhance the accessibility and cost-effectiveness of solid substrates by refining the methodology, thereby removing previous barriers to their widespread use in SERS. By optimizing the fabrication and wet-chemistry transformation into plasmonic nanostructures, this study aimed to develop a reliable and reproducible strategy for producing high-performance SERS substrates. These findings contribute to the growing field of plasmonic sensors and underscore the importance of substrate engineering in advancing molecular detection technologies. Moreover, the development of nanostar-based substrates with tunable plasmonic responses has the potential to bridge the gap between fundamental plasmonics research and practical sensing applications in biomedical and chemical analysis.

2. Results

2.1. Nanofabrication and Structural Characterization of Solid Substrates

The fabrication of the well-order and density-packed SERS substrate started with the deposition of a thin gold film onto a base substrate, followed by EBL. Using a fast exposure method, [14,15] precise nanodots were patterned onto the gold film at area exposure doses ranging from 5 to 285 $\mu C \, cm^{-2}$ and pitch values (interparticle distance) of 200, 300, 500, and 700 nm, leading to a variety of morphologies, including well-defined arrays as well as underexposed and overexposed regions. The exposure is realized by filling a rectangular area with dots following the desired pitch and resulting in an average area dose. Each dot received an individual dose calculated according to the formula: $d_{dot} = d_{area} \times p^2$ where p is the pitch. The average area dose ranged, in all the experiments resulting in individual dot doses in the range of 24 to 1400 fC. To systematically explore the fabrication limits, we nanofabricated structures at a range of doses for each pitch, ensuring a comprehensive capture of morphological transitions. These exposed

nanodots played a crucial role as masks in a subsequent carefully controlled Au etching process, selectively removing unprotected areas of gold film and producing highly ordered square superlattices of gold nanodisks on the substrate which turned into a variety of diameter-to-pitch ratios. **Figure 1**Ai–iii and vii–ix presents representative SEM images of nanostructures after Au etch with pitches of 200 and 300 nm, obtained at different exposure doses and conditions. Figures S2, S3, and S4 (Supporting Information) further illustrate these nanodisk arrays with enhanced clarity and detail.

This controlled process promoted to generate structures ranging from isolated nanodisks to closely packed structures, including merged nanodisks (or Au film with nanoholes) up to a continuous gold film. As expected, lower pitches required less dose due to proximity effects in EBL. The resulting square superlattice of gold structures served as a nanotemplate for a subsequent chemical transformation process, inducing the formation of sharp tips and additional hot spots (Figure 1Aiv-vi,x-xii). As shown in Figure S1A (Supporting Information), the fabricated plasmonic nanostar substrate was engineered with distinct columns, each defined by a different interparticle pitch. Within each column, multiple rows correspond to areas exposed to different electron beam doses. Figure S1B (Supporting Information) presents a microscope image of one such line used for SERS measurements. The wet-chemistry growth protocol, using polyvinylpyrrolidone (PVP), N,N-dimethylformamide (DMF), and HAuCl₄, was then applied transforming in a controlled way the gold nanotemplate into sharp-edged nanostructures, crucial for enhancing local electromagnetic fields and improving SERS performance. PVP acted as a stabilizing and directing agent, controlling the anisotropic growth of the nanostructures, while DMF facilitated the reduction of gold precursors, [16] ensuring a uniform deposition of gold atoms onto the nanodisks. Our approach used the patterned gold nanotemplate/disks themselves as seeds, instead of relying on a traditional gold seed solution. The resulting nanostars showed complex, irregular morphologies with numerous sharp spikes, highlighting the controlled transformation from uniform disks into multifaceted structures. This fabrication process is highly dependent on the precise control of EBL exposure doses to grow nanostructures directly from a gold film is not commonly reported in the literature. It led to four distinct configurations observed in the final nanostar substrate: i) unresolved nanostars when doses are insufficient, ii) well-defined individual nanostar superlattices with varying doses, iii) nanoholes forming when nanostar diameters closely match the pitch value, and iv) a continuous gold film with spikes forming at excessive doses. This dose-dependent modulation in morphology not only highlights the precision and versatility of our fabrication process but also underscores its potential for tailoring the properties of the SERS substrate to meet the specific requirements of diverse applications.

Figure 1B presents an analysis of individual gold nanodisks and nanostars diameters as a function of EBL exposure dose and different pitch values. These measurements, obtained via HRSEM imaging of at least 150 structures, were performed both before and after the growth process for well-defined nanostructures. Only non-merged, clearly distinguishable nanostructures were included in this analysis, as the ImageJ software was only able to accurately detect and measure isolated particles with

ADVANCED OPTICAL MATERIALS

www.advopticalmat.de

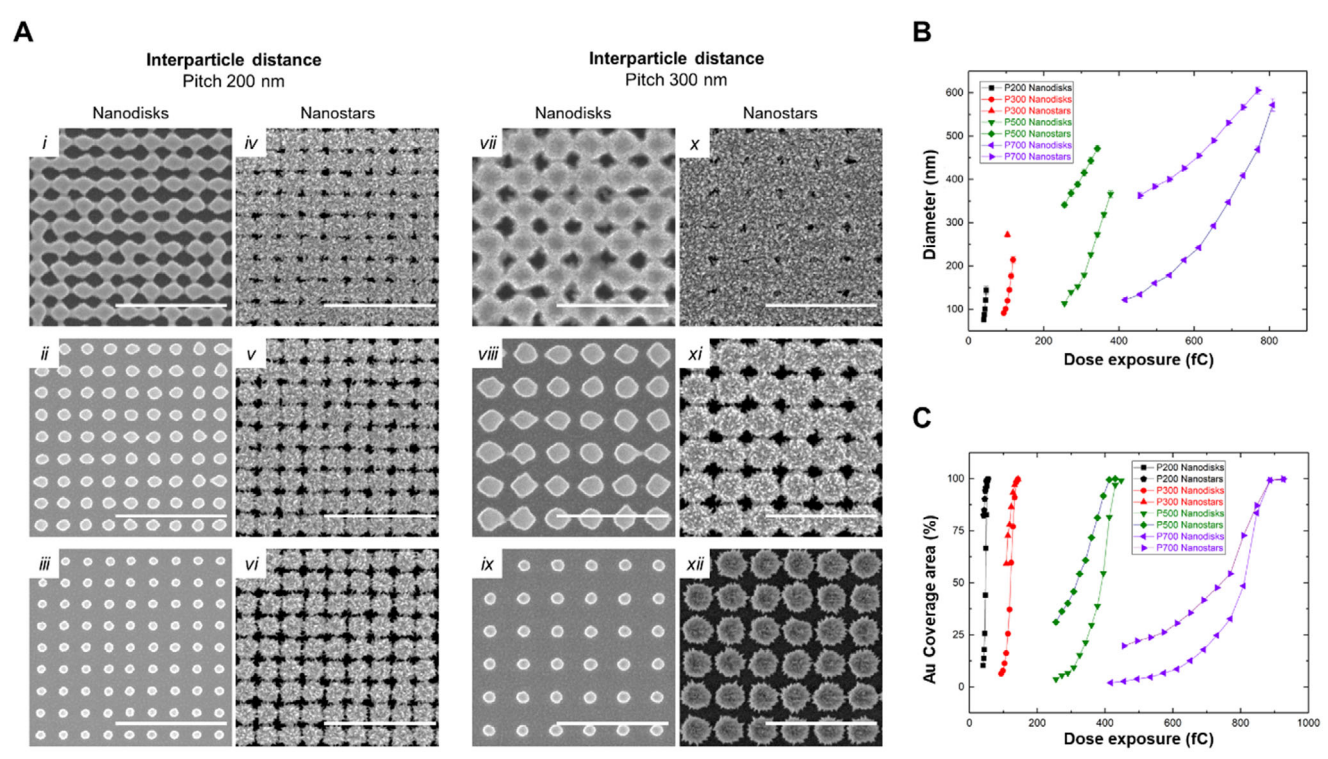


Figure 1. Structural and dimensional analysis of substrates. A) High resolution scanning electron microscope (HRSEM) images showcasing the morphological evolution of nanostructures on Au nanodisks i, ii, iii, vii, viii and ix) and their corresponding transformations after Au growth solution treatment iv, v, vi, x, xi, xii) for interparticle distances (pitch) of 200 and 300 nm. Scale bar represents 1 μ m. Parameters [dose (fC); morphology; diameter (nm); Au coverage area (%)]: i (48.4; merged nanodisks; NA; 66.5%), ii (45.2; nanodisks; 120.9 \pm 5.1; 25.8%), iii (42.0; nanodisks; 87.6 \pm 2.6; 13.7%), iv (48.4; merged nanostars; NA; 93.3%), v (45.2; nanodisks; NA; 77.9%), vi (42.0; nanodisks; NA; 59.1%), vii (128.3; merged nanodisks; NA; 77.0%), viii (118.4; nanodisks; 214.3 \pm 7.3; 37.2%), ix (103.5; nanodisks; 119.6 \pm 3.0; 11.3%), x (128.3; merged nanostars; NA; 96.9%), xi (118.4; merged nanostars; NA; 86.4%), xii (103.5; nanostars; 272.3 \pm 5.6; 59.1%). B) Measured diameter sizes of well-defined gold nanodisks templates before growth and resulting nanostars post-growth, highlighting the impact of pitch and exposure dose on final structure size. Values obtained from SEM images for at least 150 nanostructures. C) Gold surface coverage analysis of nanostructures before and after the growth process, illustrating material deposition trends and structural evolution.

defined contours. For substrates with a 200 nm pitch, all nanostars presented only merged morphologies after the growth, precluding accurate diameter measurements for this condition. For other pitch values (300, 500, and 700 nm), a clear and consistent trend was observed: increasing the electron beam dose resulted in a corresponding increase in the diameter of the nanodisks and nanostars. However, the diameter increase is not strictly linear due to proximity effects during EBL, where electrons scattered in nearby regions unintentionally increase the local dose, especially at smaller pitches. This leads to overlapping exposure and a nonlinear relationship between nominal dose and resulting feature size. The variance in diameters was remarkably low, with minimal error deviation bars, highlighting the exceptional precision and control over the morphology of these arrayed nanostructures. By comparing nanodisks and nanostars, the average diameter increases in ≈180 nm, with variations dependent on the initial diameter-to-pitch ratio (Figure 1D).

Figure 1C presents the variation in circularity measurements between nanodisks and nanostars, showing a significant reduction from 0.7–0.9 to 0.4–0.7 post-growth. This decrease underscores the morphological changes brought about by the growth process and highlights the shift from more uniform circular shapes to highly irregular, sharp protrusions that contribute to

their enhanced plasmonic properties. Figure 1C presents the topview gold coverage area (%) for all structures, before and after the growth process for each morphology. This figure illustrates the progression from low coverage to full surface gold coverage.

With the growth process, remarkable optical and structural changes were observed, such as enhanced complexity in nanostructure, and the creation of numerous Au sharp tips, which were intended for enhanced SERS performance. In some cases, we observed nanoholes decorated with surrounding gold spikes, forming what we refer to as "inverted nanostars." These structures emerge when adjacent nanostars grow toward each other, creating a central void that mimics the star-like geometry in negative. With continued growth, this process can evolve into a continuous gold film of interconnected nanostars as depicted in Figures S3,S4 (Supporting Information). This dynamic morphological evolution highlights the versatility of our fabrication method, enabling the creation of a range of nanostructures tailored for specific applications, particularly in biosensing, where high SERS performance is essential.

The produced plasmonic nanostar materials have well-characterized structural and optical differences on the basis of interparticle distances and growth. The development of well-defined nanodisks into nanostars is easily realized in diameter



www.advopticalmat.de

as well as in circularity measurements, emphasizing the wet chemistry process in nanostructure remodeling. As evident from Figure S1D (Supporting Information), at a constant growth time, the nanostar growth rate is determined by the initial diameter-to-pitch ratio, with smaller initial nanodisks undergoing greater growth. However, as nanostars reach the pitch size, lateral growth slows down, imposing a natural growth restraint before neighboring structures merge into fused nanostars. Circularity measurements (Figure S1C, Supporting Information) also confirm this conversion, where nanodisks are highly circular (\approx 0.8) initially but reduce in circularity upon chemical growth to \approx 0.6, as it forms sharp protrusions. Such morphological modification is also relevant in controlling the plasmonic nature of the substrate, achieving optimal localized field confinement and efficiency for SERS applications.

2.2. Computational Analysis of Plasmonic Enhancements

Simulations were made in Lumerical to compare the electric field enhancement of an array of nanostars compared to an equivalent array of nanodisks. FDTD simulations were used to model the electromagnetic field distribution and resonance modes of both nanodisks and nanostars. The simulations were performed to provide insights into how structural modifications impact the localized electric field enhancement and scattering properties relevant for SERS applications. Briefly, nanodisks and nanostars models were built in AutoCAD Mechanical (Figure 2A) and the model geometry was constructed in Lumerical (Figure 2B).

Simulations of nanodisks revealed well-defined plasmonic resonances modulated by interparticle spacing and diameter-to-pitch ratios, as can be seen in the reflectance spectra in Figures S5,S6 (Supporting Information). The electric field distributions exhibited symmetric and moderately enhanced fields around the nanodisks, indicative of limited coupling effects in the periodic array (Table S1, Supporting Information). In contrast, nanostars simulations showed more intense field localization at the sharp tips, indicating significantly higher enhancement factors compared to nanodisks. The presence of multiple protruding tips on the nanostars demonstrated once again an increased number of electromagnetic hotspots, making them potentially more effective for SERS applications.

A comparative analysis of the electric field intensity between nanodisks and nanostars demonstrated that nanostar tips concentrated the electromagnetic fields up to 3 orders of magnitude higher than nanodisks. These results aligned well with experimental findings, reinforcing the superior SERS performance of nanostars due to their ability to sustain stronger and more localized plasmonic fields.

Figure 2C shows a comparison of the electric field magnitude for 50 nm nanodisks compared to 75 nm nanostars at several pitch spacings. Figure 2D presents the electric field magnitude of several sizes of nanostars with compared to 50 nm nanodisks at a fixed pitch of 500 nm from the center to center of each particle. Local electric field enhancement was observed at nanostar tips. For a 500 nm pitch spacing, the maximum local electric field magnitude was obtained in the simulations of 125 nm nanostars. The enhanced electric field observed for the 125 nm nanostars likely results from an optimal combination of core size and

branch geometry, which maximizes the concentration of LSPR. At this size, the spatial distribution and sharpness of the tips may lead to more efficient coupling between nanostars and increased near-field enhancement, without the damping effects observed at larger sizes (e.g., 175–225 nm). In contrast, smaller nanostars (e.g., 75 nm) may have fewer or less pronounced branches, leading to weaker hot spots. This intermediate size thus represents a balance between size-dependent plasmonic resonance, interparticle coupling, and geometric sharpness, resulting in the highest simulated field intensities. The simulations provided critical insights into how structural modifications influence plasmonic behavior, supporting the experimental observations of improved performance in nanostar-based substrates, as well as the selection of the most suitable structures for different prospective applications.

2.3. SERS Performance Evaluation of Nanofabricated Morphologies

2.3.1. 1-Naphtalenethiol Detection Across Different Morphologies of the SERS Substrate

To assess the influence of the different SERS substrate morphologies presented in the previous section, the well-known Raman reporter molecule 1-Naphtalenethiol (1-NAT) was used. This molecule was selected due to its high Raman cross-section, chemical stability, and affinity for metal surfaces. These characteristics enable 1-NAT to form a consistent monolayer on SERS substrates. The selected characteristic peak of 1-NAT (ring stretching vibrational mode, 1372 cm⁻¹) was used to monitor the SERS performance of the different structures before and after substrate growth (using 300 nm pitch)^[17] (Figure 3A, inset). Before growth, the nanodisk arrays produced no characteristic SERS signal for 1-NAT, which can be associated to insufficient hotspot density and weak near-field enhancements caused by large interparticle distances. After the chemical growth, a very pronounced SERS signal was observed, related to the formation of sharp tips and, consequently, enhanced plasmonic coupling. After growth, different pitches (200, 300, 500, and 700 nm) and different EBL doses were analyzed based on the 1-NAT intensity for each combination. As shown in Figure 3A, all tested conditions promoted 1-NAT signal identification.

Interestingly, signal trends did not directly correlate with Au surface coverage, which would be proportional with the higher density of nanospikes per area. In the smaller pitches (200 and 300 nm) the strongest signals appeared in merged nanostar morphologies, indicating that controlled plasmonic coupling enhances rather than diminishes local field intensities. The presence of sharp tips, even protruding to nanohole areas, seems to facilitate strong electromagnetic confinement and likely contribute to further field enhancement. In contrast, for larger pitches (500 and 700 nm), the highest signals were observed in well-spaced nanostars, where merging led to field delocalization, reducing enhancement effects. The highest signal intensity was observed in the 300 nm pitch (dose 118.4 fC). This configuration likely provided the best balance between hot spot density and molecular accessibility, optimizing the localized electromagnetic field.

21951071, 0, Downloaded from https://advanced.onlinelibrary.wiley.com/doi/10.1002/adom.202501275 by Cochrane France, Wiley Online Library on [08/10/2025]. See the Terms and Conditions (https://onlinelibrary.wiley.com/terms

-and-conditions) on Wiley Online Library for rules of use; OA articles are governed by the applicable Creative Commons License



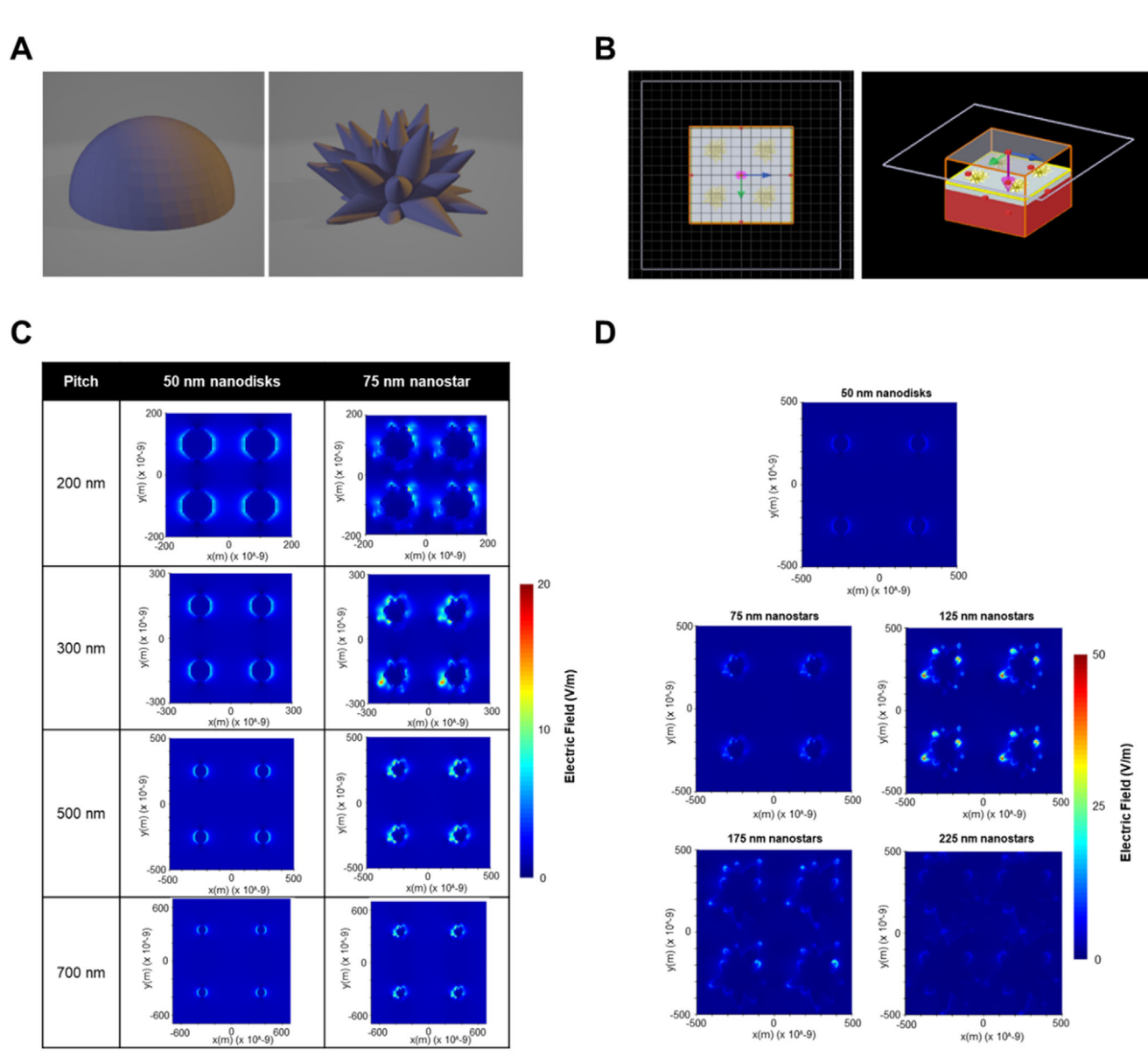


Figure 2. Lumerical simulation setup and results for nanodisk and asymmetric nanostar geometries. A). STL files of (left) nanodisk and (right) asymmetric nanostars to show the geometry of the features imported into Lumerical for simulation. B) Lumerical simulation area setup: (Left) diagram/top-down view of the 75 nm nanostars on a substrate with a 500 nm pitch distance. Grid square is 100 nm × 100 nm; (Right) 3D diagram of Lumerical setup, where the red region represents silicon, the grey region represents silicon oxide, the yellow stars represents gold, and the orange box outlines the FDTD simulation area. The white box indicates the source location. C) Simulation results showing electric field magnitudes for 50 nm nanodisks and 75 nm nanostars at different pitch spacings. D) Simulation results demonstrating local field magnitude at the sharp tips of nanostars of several sizes compared to nanodisks of 50 nm.

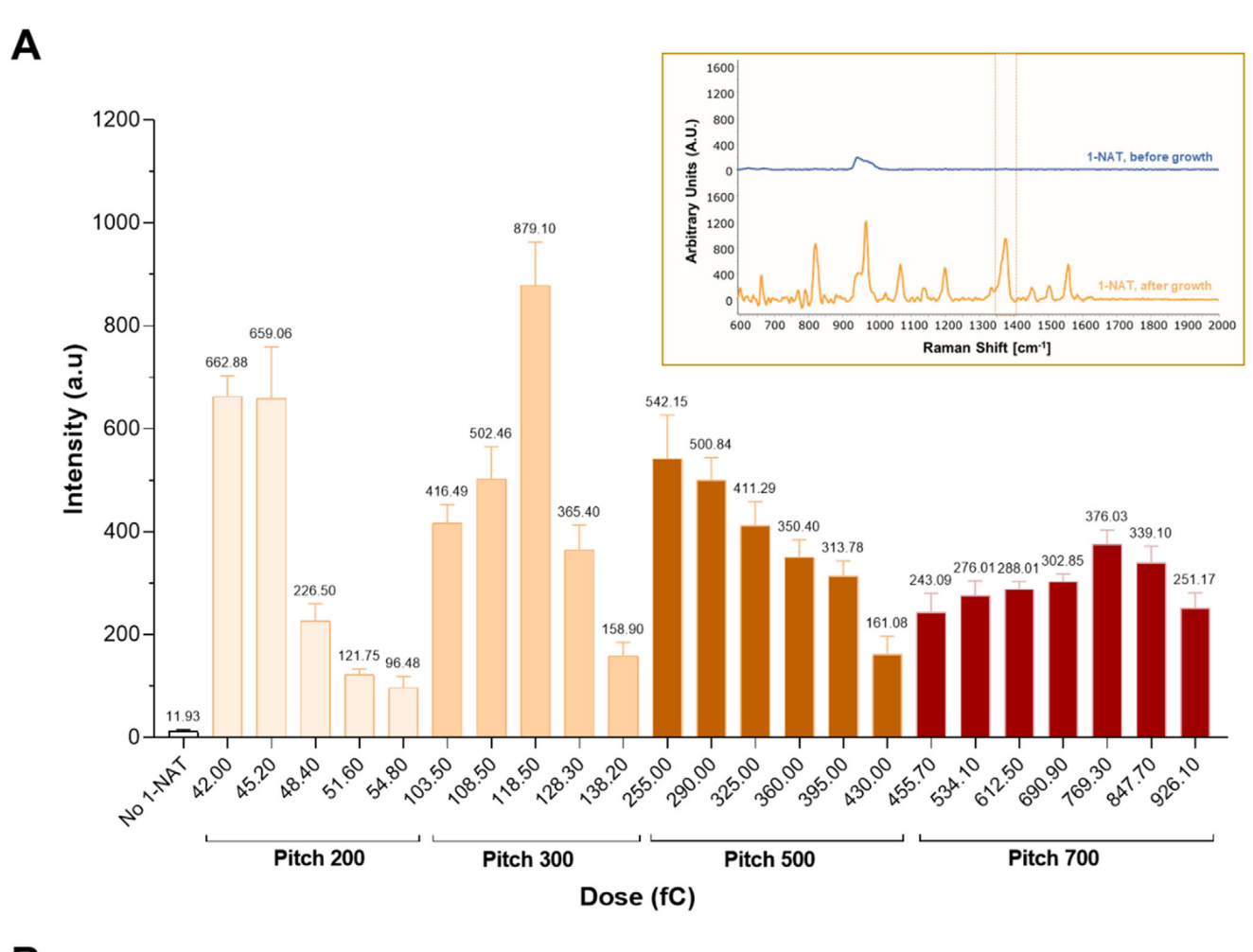
Figure 3B shows the SERS mapping based on the intensity of the 1372 cm⁻¹ 1-NAT peak, demonstrating consistent high signal homogeneity and reproducibility across different pitches. This phenomenon underscores the importance of fine-tuning substrate geometries to promote a careful balance between plasmonic coupling and hot spot density, to achieve optimal SERS performance. Overall, these results emphasize the critical influence of substrate selection on SERS signal enhancement, validating the potential of substrates for sensitive and precise biomarker detection.

2.3.2. Assessment of SERS Signals of 1-NAT and Tryptophan Across Varying Concentrations

To further investigate the analytical performance of the SERS substrates across, a range of concentrations of 1- NAT, spanning from 10^{-14} to 10^{-4} m, were tested using the optimized 500 nm pitch merged nanostars substrate (Figure S1B, Supporting Information). Figure 4A revealed a concentration-dependent SERS signal intensity for 1-NAT, with the strongest signals observed at 10^{-4} M, as expected. The signal of 1-NAT could be observed in

21951071, 0, Downloaded from https://advanced.onlinelibrary.wiley.com/doi/10.1002/adom.202501275 by Cochrane France, Wiley Online Library on [08/10/2025]. See the Terms and Conditions (https://onlinelibrary.wiley.com/doi/10.1002/adom.202501275 by Cochrane France, Wiley Online Library on [08/10/2025]. See the Terms and Conditions (https://onlinelibrary.wiley.com/doi/10.1002/adom.202501275 by Cochrane France, Wiley Online Library on [08/10/2025]. See the Terms and Conditions (https://onlinelibrary.wiley.com/doi/10.1002/adom.202501275 by Cochrane France, Wiley Online Library on [08/10/2025]. See the Terms and Conditions (https://onlinelibrary.wiley.com/doi/10.1002/adom.202501275 by Cochrane France, Wiley Online Library on [08/10/2025]. See the Terms and Conditions (https://onlinelibrary.wiley.com/doi/10.1002/adom.202501275 by Cochrane France, Wiley Online Library on [08/10/2025]. See the Terms and Conditions (https://onlinelibrary.wiley.com/doi/10.1002/adom.202501275 by Cochrane France, Wiley Online Library on [08/10/2025].

and-conditions) on Wiley Online Library for rules of use; OA articles are governed by the applicable Creative Commons License



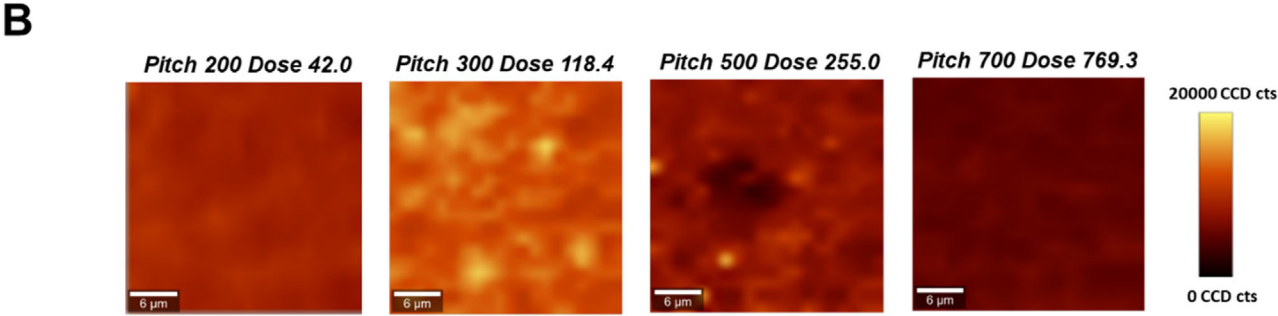


Figure 3. Evaluation of SERS substrates performance and homogeneity. SERS spectra resulting from measurement with 10⁻⁴ m of 1-NAT: A) Comparison of average SERS intensities across different doses and pitches (200, 300, 500, and 700 nm) after growth, measured over a 30 μ m \times 30 μ m mapped area (400 spectra). Inset: comparison of the SERS substrates before and after the growth process. The SERS spectrum is an average of 400 spectra from a map. Map area: 30 μm × 30 μm, 1.5 μm step size. The characteristic peak of 1-NAT (1372 cm⁻¹) is highlighted with a box. B) SERS intensity map highlighting the highest-performing line in each pitch and dose. Laser wavelength: 785 nm; Laser power: 10 mW; Objective: 50x.

concentrations as low as 10^{-14} M, indicating the substrate's capacity for very ultrasensitive molecular detection. These insights are vital for understanding the substrate's sensitivity limits, homogeneity, and its optimal working concentration range and, consequently, the potential for applications in biomarker detection.

As a further proof-of-concept to assess the substrate's ability toward ultrasensitive detection, the molecule tryptophan was tested. Tryptophan is an essential biomolecule involved in metabolic and physiological processes and particularly relevant in cancer research and diagnostics, where tryptophan metabolism plays a key role in tumor progression and immune escape.[18] Different concentrations of tryptophan (10⁻² and 10^{-4} M) were tested using the optimized SERS substrates (Figure 4Bi,ii). Figure 4B shows the SERS signal of the different concentrations and the characteristic SERS peak of tryptophan at ≈1011 cm⁻¹ (ring breathing mode) was clearly identified. SERS



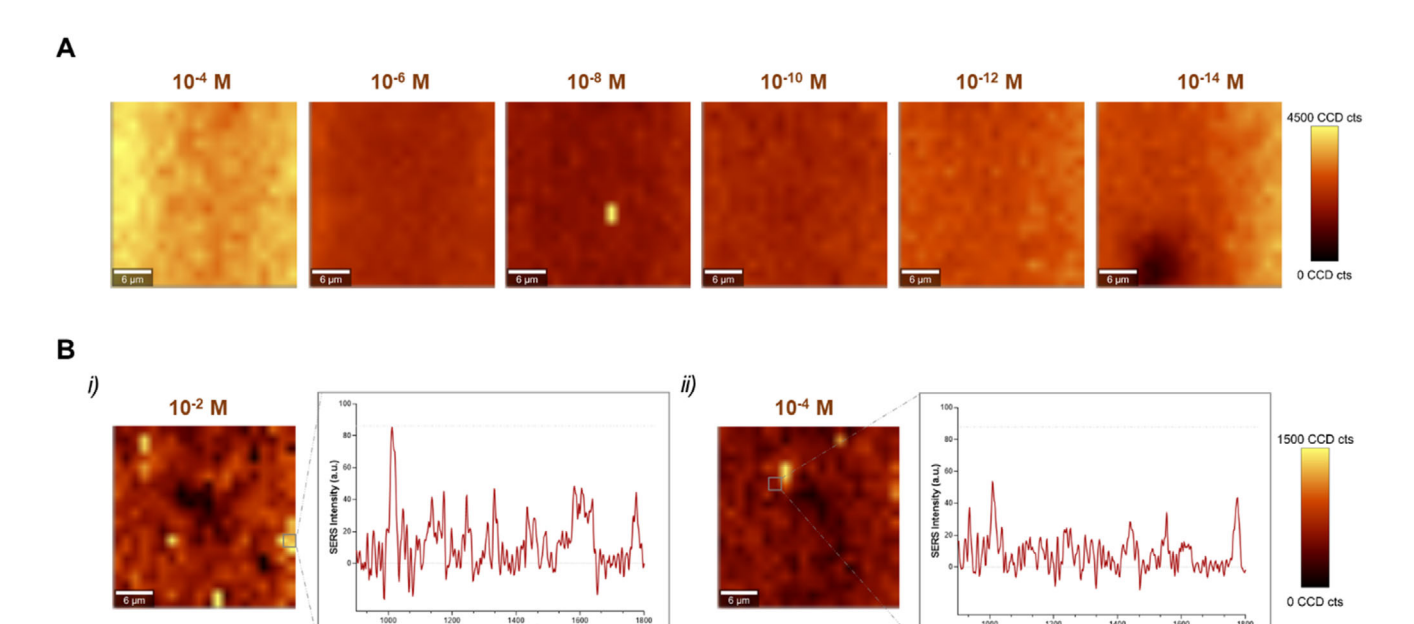


Figure 4. Performance of gold nanostar SERS substrate at different concentrations of 1-NAT and proof-of-concept using tryptophan. A) SERS spectra resulting from measurements with 1-NAT at different concentrations: 10^{-4} , 10^{-6} , 10^{-8} , 10^{-10} , 10^{-12} , and 10^{-14} M on pitch 500 nm after growth. SERS intensity map obtained for different concentrations, showing an intensity gradient. The SERS spectrum shown in each condition corresponds to a single high-intensity spot in the mapped area (25 μ m \times 25 μ m, 4 μ m step size, 1 s acquisition). The 1372 cm⁻¹ peak was selected for analysis. Range of 35. Laser: 785 nm; Laser power: 25 mW; Objective: 50x. B) SERS mapping of the substrates after immersion in tryptophan at concentrations: i) 10^{-2} and ii) 10^{-4} M. The SERS spectrum shown in each condition corresponds to a single high-intensity spot in the mapped area (25 μ m \times 25 μ m, 1.5 μ m step size, 1 s). The specific peak from tryptophan selected to result these maps was 1011 cm⁻¹, with a range of 30. Laser: 785 nm; Laser power: 10 mW; Objective: 50x; Scale 6 μ m.

mapping revealed widespread higher-intensity regions (indicated by intense yellow in the color maps), confirming the uniformity of hotspot distribution.

3. Discussion

The development of these novel SERS solid substrates allowed precise control of interparticle distances, enabling highly controlled enhancement factors and greater signal intensity and uniformity. The precision level offered by these solid substrates has potential for accurate detection and analysis of challenging molecules or biomarkers. Despite the common perception that SERS substrates fabricated via EBL are costly, our work challenges this notion by optimizing and streamlining the methodology to significantly reduce process times and production costs while maintaining high precision and scalability. The optimized exposure method achieves rapid and efficient patterning, completing four different pitches and doses in under 12 min at a typical speed of 54.27 min cm⁻². For a standard sensor area of $300 \times 300 \ \mu m^2$, the EBL exposure takes only 2.93 s, highlighting the potential of this approach for scalable, high-sensitivity, and cost-effective SERS substrate This efficiency is demonstrated through the dot-on-the-fly (DOTF) EBL technique, which significantly improves patterning speed, decreasing costs and making EBL a more viable option for nanofabrication of these types of nanostructures.[14,15] While traditional EBL has not yet experienced widespread use on a large-scale industrial basis, the improved rapid-exposure process described here makes the technique useful for the manufacture of larger substrates. Moreover, other scaling techniques, such as deep ultraviolet (DUV) lithography or nanoimprint lithography, typically applied to microprocessor manufacture, represent legitimate options for bringing production up-scale while keeping costs low. By contrast, purely wet chemistry-based fabrication of SERS substrates is typically plagued by low precision. This is most likely to lead to uneven surface coating, nanoparticle agglomeration, and chemical contamination risks. These drawbacks negatively influence reproducibility and uniformity, thus making it difficult to attain controlled, scalable production, one of the key challenges addressed in this area of study. But by tackling these issues head-on, our approach offers a more reproducible and scalable means of producing high-performance SERS substrates.

These substrates were fabricated using a two-step process: i) an EBL-fabricated Au nanotemplate and ii) a chemical growth process with controlled growth to create nanostars, where nanostar formation allows controlled hot spot generation necessary for obtaining highly intense SERS signals. Other works demonstrated the potential of combining fabrication methods to enhance nanostructured arrays. For example Neretina et al.[19] and Hughes et al.^[20] also studied hybrid approaches that applies the microfabrication approach and chemical growth as complementary procedures to produce optimized nanostructured arrays of metallic nanoparticles, like Au@Ag prisms, Au@Ag cubes, and Au@Ag nanoshells and nanocages, among others.[19] In a recent paper Demille et al.[21] reported the production of a large area periodic array of gold nanostars by using substrate-supported Au seeds (obtained through a lift-off procedure) immersed in a reducing DMF+PVP+HAuCl₄ solution. Other strategies





www.advopticalmat.de

underscore the broad interest in and potential for tailored nanostructures to enhance SERS sensitivity and expand its applications. For example, Li et al. proposed a broadband porous Ag-Au nanoparticle array, using an ultra-thin alumina mask (UTAM) technique to create arrays with big hotspots for SERS.^[22] Peng et al. produced Ag-coated gold nanorod arrays with tunable plasmonic properties, with effective results in the detection of antibiotics through effective plasmonic coupling among nanoparticles.^[23] In addition, another study using an Au-Ag nanoparticle array sandwiched, integrated into an adhesive acrylic polymer tape and a polyethylene terephthalate film resulted in a high-performance SERS chip for pesticide detection.^[24]

The efficiency and homogeneity of the herein presented SERS substrates was initially demonstrated using 1-NAT (Figure 3), providing a benchmark for comparing substrate performances, [25] highlighting the robustness of our approach. This performance is promising for the detection of more complex molecules, such as cancer biomarkers and amino acids, exemplified by the successful detection of tryptophan (Figure 4B). Tryptophan detection is relevant in biomedical research due to its role in immune response and tumor growth pathways. [26] Real-time monitoring of tryptophan levels in biological samples can thus provide insights into the tumor microenvironment and immune system interactions. The challenge of detecting tryptophan through SERS is due to its weak adsorption to gold surfaces. Unlike thiol-containing molecules, which form strong covalent bonds with gold, tryptophan binds through weaker π – π stacking interactions via its indole ring. Additionally, the amino and carboxyl groups in tryptophan may contribute weak electrostatic forces, although these are not as significant as the π - π interactions. The effectiveness of this interaction is influenced by the orientation and proximity of the molecules to the gold surface and consequently results in variable SERS signal intensities. This relatively weaker interaction, compared to thiolcontaining molecules like 1-NAT, makes tryptophan a less common choice for SERS studies involving gold surfaces. According Kandakkathara et al. the relative intensities of the tryptophan peaks in the SERS spectrum are dependent on several factors (e.g., the metal used, colloid aggregation, and pH).[27] These results signify the versatility and reliability of our substrates, laying a strong foundation for their utilization in diverse and complex detection scenarios, particularly in the field of cancer research and molecular analysis.

In conclusion, our optimized SERS substrates provided good accuracy and efficiency, with the capacity to produce homogeneous and intense signals across different molecules. Their demonstrated sensitivity and reproducibility make them as promising tools for advancing complex detections, particularly in the exploration of cancer biomarkers and intricate molecular interactions.

4. Conclusion

This work introduces a new, scalable, and cost-effective method of fabricating high-performance SERS substrates through an optimized process of EBL followed by controlled chemical growth. In working with rapid exposure times and fine capabilities, we challenge the widespread perception that top-down fabrication

such as EBL is too impractical for use at a large scale. A precise nanopatterning was integrated with chemical growth demonstrating nanostar arrayed geometries with significantly improved electromagnetic field localization, a parameter controlling high-intensity SERS signals.

The controlled chemical synthesis process enabled the control of interparticle spacing, nanoparticle architecture, and substrate homogeneity in a systematic manner, providing enhanced reproducibility and signal homogeneity. The research also emphasizes the effect of substrate geometry on SERS amplification and its role in obtaining larger magnitudes of signals through the optimization of nanostructure geometries.

Our findings demonstrate the capabilities of scalable and precise nanofabrication to propel SERS-based sensing technologies. Though our approach sets a good foundation for building reproducible and durable SERS platforms, future studies must explore other surface functionalization and integration with large-scale fabrication techniques such as nanoimprint lithography or DUV lithography in order to further enhance manufacturability. In general, this work is a milestone in bridging the gap between high-precision nanofabrication and practical SERS application, particularly in molecular sensing and biological diagnosis.

5. Experimental Section

Plasmonic Nanotemplate Fabrication: The fabrication of the nanodisks template followed a precise nanofabrication workflow to ensure high reproducibility and structural integrity. First, a 100 nm thick SiO₂ layer was deposited by plasma-enhanced chemical vapor deposition (PECVD) on a single-side polished (SSP) (1 0 0) 200 mm Si wafer or Si sample (30 × 30 mm²) (p-type, boron doped, (1 0 0), 725 μm thickness (1-100 Ω-cm) from Silicon Valley Microelectronics, Inc.). Next, a metallic stack composed of 3 nm Cr and 100 nm Au was deposited by multi-target sputtering (Kenosistec). This was followed by physical vapor deposition (PVD) of a 20 nm Al₂O₃ layer (Singulus, Timaris FTM) to protect the Au surface during further processing. To promote resist adhesion, the wafer was treated with hexamethyldisilazane (HDMS) vapor (Sigma–Aldrich), followed by spin coating of 160 nm AR-N 7520.18 electron beam resist (Allresist GmbH).

The EBL patterning was carried out using a Vistec EBPG 5200 (Raith GmbH) with pitches of 200, 300, 500, and 700 nm via the dots-on-the-fly (DOFT) method with a beam with 100 kV voltage and 50 nA. Each patterned areas was 2 mm in width and 80 µm in height for each EBL dose. Each area was exposed using dot arrays, where individual dots received varying dwell times to precisely control the local dose at each position. After EBL exposure, the resist was soft-baked at 85 °C for 120 s, followed by a post-exposure bake at 85 °C for 60 s, and developed in AR 300.47 (3:4 in water) using six 30 s cycles at room temperature, with intermediate rinsing and final spin-drying at 4000 rpm. The patterned structures, consisted in Si / 100 SiO_2 / 3 Cr / 100 Au / $20 \text{ Al}_2 \text{O}_3$ / 160 resist (with nanofilms thickness in nm), were then transferred into the alumina and gold layer using an ion beam milling system (Nordiko Ion Milling 7500, UK). The Argon ion milling process used an argon plasma source with a 130° etch angle (depending on geometry), and sidewall cleaning at 165°, 30 rpm rotation for uniformity (typically <5% across the wafer), with etch rates $\approx 10 \text{ nm min}^{-1}$ depending on the material and geometry (typical example reference is of 16.67 nm/min for SiO₂). The process endpoint stopping at 50% of the Cr peak was detected via an integrated secondary ion mass spectrometry (SIMS) module. The remaining resist was removed using an oxygen plasma (Tepla PVA GIGAbatch 360 M, USA), and the protective Al₂O₃ layer was stripped using AZ400K (Microchemicals GmbH, Germany). To finish, the wafer was rinsed with deionized water and dried (SÜSS MicroTec AG, Germany), followed by automated dicing into individual chips using the Disco DAD 3500 dicing system (USA). The gold nanodisk templates used as seeds in this study were originally developed



www.advopticalmat.de

Table 1. Pitch spacings and comparable nanostar/nanosphere models.

Pitch [nm] centre-to-centre	Radius [nm] nanodisk	Radius [nm] nanostar
200	50	75
300	50	75
500	50	75
700	50	75
500	50	75
500	50	125
500	50	175
500	50	225
500	50	275

during the GRAPHSENS (FCT, POCI-01-0145-FEDER-028114) and TAR-GET (FCT, UTA-EXPL/NPN/0038/2019) projects and subsequently optimized and adapted for the current fabrication protocol and application.

Growth of Nanostars Tips on Top of Nanoplates: Nanostar tips were grown directly on the lithographically patterned gold nanotemplate using a very common protocol combining: N, N-dimethylformamide (DMF), PVP, and chloroauric acid (HAuCl₄). In this work, the gold nanodisks were used as "seeds." Thus, 10 g of PVP-10K were dissolved in 100 mL of DMF using an ultrasound sonicator for 15 min. Then, a final concentration of 0.5 mm of HAuCl₄ was added under vigorously magnetically stirring for 2 min. Afterward, the substrates were washed three times with isopropanol (IPA) to remove excess PVP and DMF and dried carefully with a nitrogen gun.

Scanning Electron Microscopy (SEM): High resolution scanning electron microscopy (HRSEM) was performed to determine the morphologies of structures and homogeneity. At each step, high-resolution imaging of the synthesized substrates was done using a NovaNanoSEM 650 microscope (5 kV, high vacuum), and multiscale magnifications were employed for examining the shape of the nanodisk, the nanostar tip extension, and surface coverage in general.

ImageJ FIJI Semi-Automated Analysis: Image analysis and processing were performed using FIJI (ImageJ). A minimum of 150 nanodisks and nanostars were processed to ensure statistically robust characterization for size distribution, shape uniformity, and surface coverage areas. Scale bars were utilized to calibrate the SEM images, and the noise was reduced and threshold corrected. Automated particle analysis tools were used to calculate the diameters of the nanostars, circularities, and Au coverage area quantification was achieved through image segmentation and measurement of occupied Au top-view surface fractions.

Finite-Difference Time-Domain (FDTD) Simulations: To gain a better understanding of the optical properties of the nanodisks and nanostars that are synthesized, FDTD simulations were performed in Lumerical. In Lumerical, a model area was constructed with a 500 nm high silicon base, on top of which a thin 100 nm high silicon oxide (SiO2) layer was placed. Four gold nanostars or nanospheres were placed in a 2 \times 2 array on this substrate with pitch spacing according to Table 1. A 400 nm high block of air was simulated above the substrate. The width of each simulation was twice the pitch spacing in both X and Y to produce a symmetric array condition. All materials used the Palik refractive index data for modelling.

The calculations were used to compute the distribution of electric fields around the nanostructures and to predict the influence of morphology on the electric field enhancement. Boundary conditions were considered as perfectly matched layers to prevent nonphysical reflection. Dielectric constants of gold were also retrieved from built in material parameters, and the source of excitation was established as a plane wave of 785 nm wavelength to align with Raman experimental conditions. Electric field enhancement maps were calculated in comparison to a pit against nanodisk and nanostar geometries.

Briefly, nanodisks and nanostars models were built in AutoCAD Mechanical and sliced in half to retain the upper half of the star to simulate an embedded condition on the substrate. These were exported as STL files for

import into Lumerical. To emulate the asymmetrical nature of the nanostars, a 31-spike symmetrical nanostar was first constructed in AutoCAD, and then the spike size was scaled by a random number to be between 85% and 115% of the initial set size. Spike tips were rounded to avoid non-physical inhomogeneities in the simulated electric field, and reflect typical rounding seen in colloidal and fabricated nanostars. The spike angle was rotated at a random angle of up to 20° in a random direction from the baseline symmetrical model to have similar morphologies.

Boundaries in the Z direction had PML boundary conditions. The source wave was a 785 nm plane wave with an amplitude of 1 and Bloch/periodic conditions, fully polarized with 0° rotation, directed in the -Z direction. Monitors (to measure the electric field) were placed in the plane of the surface of the SiO_2 layer, and at 5, 10, and 15 nm above the plane.

1-NAT and Tryptophan Solutions for Raman Signal Inspection: After the tip growth, a Raman reporter, 1-naphthalenethiol (1-NAT), was used to test the potential of the substrates. For that, the different substrates (before and after growth) were immersed in a solution of 1-NAT with a concentration of 10^{-4} m in ethanol. The incubation time was 2 h under shaking followed by 3 washes with ethanol and dried carefully with a nitrogen gun. The different pitches and doses lines were measured in order to determine the most effective configuration. Once identified, the optimal and same substrate was used for the calibration curve and different increasing concentrations of 1-NAT, in ethanol, were used: 10^{-14} , 10^{-12} , 10^{-10} , 10^{-18} , 10^{-6} and 10^{-4} m.

Additionally, different concentrations of tryptophan: 10^{-4} and 10^{-2} M, in MilliQ water, were also tested. For both solutions, the substrates were immersed during 2 h under gentle shaking, carefully washed (only for 1-NAT), carefully dried, and analyzed.

SERS Analysis: Raman measurements were carried out in a 300R Confocal Raman microscope (WITec) using a 785 nm laser and a 600 gr-cm $^{-1}$ grating as the excitation source. SERS maps of the substrates were acquired with a 50× objective at a 1.5 μ m step size and an acquisition time of 1 s. SERS spectra were processed with the Project4 WITec software for background and cosmic ray removal corrections and Spectragryph software for figure preparation.

Supporting Information

Supporting Information is available from the Wiley Online Library or from the author.

Acknowledgements

This work was financially supported by the European Innovation Council (Horizon 2020 Project: 965018—BIOCELLPHE); by the EU under the program HORIZON-EIC-2022-PATHFINDEROPEN-01-01 (ga 101099066) and by the UK Research and Innovation (UKRI) under the UK government's Horizon Europe funding guarantee (ga 10063360- 3DSecret) and by the Health From Portugal project (C630926586-00465198), supported by Component C5 - Capitalisation and Business Innovation, under the Portuguese Resilience and Recovery Plan, through the NextGenerationEU Fund. Part of the initial nanotemplate development work was supported by the Portuguese Foundation for Science and Technology (FCT) through projects GRAPHSENS (POCI-01-0145-FEDER-028114; PTDC/FISMAC/28114/2017) and TARGET (UTA-EXPL/NPN/0038/2019). A.T. acknowledges the FCT studentship SFRH/BD/148091/2019. A.C. acknowledges support from the MSCA Postdoctoral Fellowship funded by the European Union's Horizon Europe research and innovation programme under grant agreement No. 101109728 (Project SIREN). We acknowledge Dr Miguel Spuch Calvar for his contributions to the design of the 3D schemes in the table of contents.

Conflict of Interest

All authors declare no conflict of interest.

are governed by the applicable Creative Commons License

ADVANCED SCIENCE NEWS

www.advancedsciencenews.com



www.advopticalmat.de

Author Contributions

A.C., L.D., and S.A.-C. contributed to conceptualization and ideation. A.C., S.A.-C., and L.D. designed the experimental strategy; A.C., J.B., A.T., and D.M. contributed in the fabrication, growth, and SEM analysis of the substrates. T.D. contributed with simulations. A.C., A.T., J.B., D.M., M.S.R., M.A. contributed to the experimental execution of the work and data interpretation, A.C., A.T., S.A.-C. contributed to the original draft preparation, original draft revision; and all authors contributed to the final revision of the manuscript before submission. All authors have read and agreed to the final version of the manuscript.

Data Availability Statement

The data that support the findings of this study are available from the corresponding author upon reasonable request.

Keywords

EBL, microfabrication, nanoarrays, nanosensors, surface-enhanced Raman scattering spectroscopy (SERS)

Received: April 22, 2025 Revised: July 11, 2025 Published online:

- [1] J. Langer, D. Jimenez de Aberasturi, J. Aizpurua, R. A. Alvarez-Puebla, B. Auguié, J. J. Baumberg, G. C. Bazan, S. E. J. Bell, A. Boisen, A. G. Brolo, J. Choo, D. Cialla-May, V. Deckert, L. Fabris, K. Faulds, F. J. García de Abajo, R. Goodacre, D. Graham, A. J. Haes, C. L. Haynes, C. Huck, T. Itoh, M. Käll, J. Kneipp, N. A. Kotov, H. Kuang, E. C. Le Ru, H. K. Lee, J.-F. Li, X. Y. Ling, et al., ACS Nano 2020, 14, 28.
- [2] K. Kneipp, Y. Wang, H. Kneipp, L. T. Perelman, I. Itzkan, R. R. Dasari, M. S. Feld, *Phys. Rev. Lett.* **1997**, *78*, 1667.
- [3] M. Moskovits, Rev. Mod. Phys. 1985, 57, 783.
- [4] K. Oliveira, A. Teixeira, J. M. Fernandes, C. Lopes, A. Chícharo, P. Piairo, L. Wu, L. Rodríguez-Lorenzo, L. Diéguez, S. Abalde-Cela, Adv. Opt. Mater. 2023, 11, 2201500.
- [5] A. Y. F. Mahmoud, A. Teixeira, M. Aranda, M. S. Relvas, S. Quintero, M. Sousa-Silva, A. Chícharo, M. Chen, M. Hashemi, J. B. King, J. W. Tunnell, C. Morasso, F. Piccotti, F. Corsi, M. Henriksen-Lacey, D. J. de

- Aberasturi, D. Méndez-Merino, A. Rodríguez-Patón, S. Abalde-Cela, L. Diéguez, *TrAC Trends Analyt. Chem.* **2023**, *169*, 117311.
- [6] R. D. Neal, R. A. Hughes, A. S. Preston, S. D. Golze, T. B. Demille, S. Neretina, J. Mater. Chem. C Mater. 2021, 9, 12974.
- [7] K. Srivastava, H. Le-The, J. J. A. Lozeman, A. van den Berg, W. van der Stam, M. Odijk, Micro Nano Eng. 2024, 23, 100267.
- [8] V. G. Kravets, A. V. Kabashin, W. L. Barnes, A. N. Grigorenko, *Chem. Rev.* 2018, 118, 5912.
- [9] G. A. Vinnacombe-Willson, Y. Conti, S. J. Jonas, P. S. Weiss, A. Mihi, L. Scarabelli, Adv. Mater. 2022, 34, 2205330.
- [10] S. J. Lee, H. Jang, D. N. Lee, Nanoscale Adv. 2023, 5, 5165.
- [11] Á. I. López-Lorente, Anal. Chim. Acta 2021, 1168, 338474.
- [12] X.-M. Lin, Y. Cui, Y.-H. Xu, B. Ren, Z.-Q. Tian, Anal. Bioanal. Chem. 2009, 394, 1729.
- [13] K. Ge, Y. Hu, G. Li, Biosensors 2022, 12, 941.
- [14] B. Vermang, J. T. Wätjen, C. Frisk, V. Fjällström, F. Rostvall, M. Edoff, P. Salomé, J. Borme, N. Nicoara, S. Sadewasser, *IEEE J. Photovolt.* 2014, 4, 1644.
- [15] J. Trasobares, F. Vaurette, M. François, H. Romijn, J.-L. Codron, D. Vuillaume, D. Théron, N. Clément, Beilstein J. Nanotechnol. 2014, 5, 1918.
- [16] P. Senthil Kumar, I. Pastoriza-Santos, B. Rodríguez-González, F. Javier García de Abajo, L. M. Liz-Marzán, Nanotechnology 2008, 19, 015606.
- [17] R. A. Alvarez-Puebla, D. S. Dos Santos Jr, R. F. Aroca, Analyst 2004, 129, 1251.
- [18] C. Xue, G. Li, Q. Zheng, X. Gu, Q. Shi, Y. Su, Q. Chu, X. Yuan, Z. Bao, J. Lu, L. Li, Cell Metab. 2023, 35, 1304.
- [19] S. Neretina, R. A. Hughes, K. D. Gilroy, M. Hajfathalian, Acc. Chem. Res. 2016, 49, 2243.
- [20] R. A. Hughes, E. Menumerov, S. Neretina, Nanotechnology 2017, 28, 282002.
- [21] T. B. Demille, R. A. Hughes, N. Dominique, J. E. Olson, S. Rouvimov, J. P. Camden, S. Neretina, *Nanoscale* 2020, 12, 16489.
- [22] K. Li, G. Liu, S. Zhang, Y. Dai, S. Ghafoor, W. Huang, Z. Zu, Y. Lu, Nanoscale 2019, 11, 9587.
- [23] X. Peng, D. Li, Y. Li, H. Xing, W. Deng, J. Mater. Chem. B 2021, 9, 1123.
- [24] K. Wang, D.-W. Sun, H. Pu, O. Wei, *Talanta* **2021**, *223*, 121782.
- [25] E. Le Ru, P. Etchegoin, Principles of Surface-Enhanced Raman Spectroscopy: And Related Plasmonic Effects, Elsevier, Amsterdam, Netherlands 2008.
- [26] C. A. Opitz, L. F. Somarribas Patterson, S. R. Mohapatra, D. L. Dewi, A. Sadik, M. Platten, S. Trump, Br. J. Cancer 2020, 122, 30.
- [27] A. Kandakkathara, I. Utkin, R. Fedosejevs, Appl. Spectrosc. 2011, 65, 507.